Journal of Physics:
Condensed Matter

PURPOSE-LED PUBLISHING™

PAPER • **OPEN ACCESS**

The magneto-mechanical coupling of multiphase magnetorheological elastomers

To cite this article: Edward J Barron III *et al* 2025 *J. Phys.: Condens. Matter* **37** 135101

OPEN ACCESS
IOP Publishing
Journal of Physics: Condensed Matter
J. Phys.: Condens. Matter **37** (2025) 135101 (14pp)
https://doi.org/10.1088/1361-648X/adac23

The magneto-mechanical coupling of multiphase magnetorheological elastomers

Edward J Barron III[1,2,3,5], **Ella T Williams**[1,5], **Nathan Lazarus**[4] and **Michael D Bartlett**[1,2,*]

[1] Mechanical Engineering, Soft Materials and Structures Lab, Virginia Tech, Blacksburg, VA 24061, United States of America
[2] Macromolecules Innovation Institute, Virginia Tech, Blacksburg, VA 24061, United States of America
[3] Virginia Tech National Security Institute, Virginia Tech, Blacksburg, VA 24061, United States of America
[4] Electrical and Computer Engineering Department, University of Delaware, Newark, DE 19716, United States of America

E-mail: mbartlett@vt.edu

Received 2 October 2024, revised 14 January 2025
Accepted for publication 20 January 2025
Published 31 January 2025

Abstract

Magnetorheological elastomers (MREs) are soft magnetic composites that achieve tunable changes in stiffness and damping in the presence of a magnetic field. Rigid particle composite (RC) MREs have been studied for decades for their potential applications to automotive dampers and robotic systems. Recently, magnetic fluid composite (FC) MREs have been developed which utilize magnetic fluids as inclusions to elastomers. An investigation into how inclusion phase affects magneto-mechanical performance may greatly improve MRE design capabilities. Here we experimentally evaluate the impact of solid and liquid magnetic inclusions on MRE properties, construct a simple model that captures the performance of diverse MRE material architectures, and demonstrate the use of the model to create material design maps relating the material structure, zero-field properties, and applied field to the elastic modulus and specific loss. The magneto-mechanical response is evaluated for three material architectures: RC, FC, and hybrid composite MREs that use solid particles, magnetic fluids, and a combination of the two as inclusions respectively. The model is developed through magnetic and mechanical energy principles, which suggests that the phase of the magnetic inclusions impacts the change in energy density during deformation. We show that the magneto-mechanical coupling factor is dependent on the zero-field properties of the composites, which allows for the development of material design maps to inform the fabrication of MREs based on desired properties.

[5] These authors contributed equally to this work.
[*] Author to whom any correspondence should be addressed.

Supplementary material for this article is available online

Keywords: magnetorheological elastomers, magnetic elastomers, multi-phase, magnetic fluids, magnetic composites, energy dissipation, stiffness tuning

Acronyms

FC	Magnetorheological fluid composite
HC	Hybrid composite
MR	Magnetorheological
MRE	Magnetorheological elastomer
MRF	Magnetorheological fluid
RC	Rigid particle composite

Mathematical symbols

B	Magnetic flux density
B_{sat}	Saturation flux density
C_E	Magneto-mechanical coupling factor for elastic modulus
$C_{W,\text{D}}$	Magneto-mechanical coupling factor for dissipation
$C_{W,\text{L}}$	Magneto-mechanical coupling factor for loading
$C_{W,x}$	Magneto-mechanical coupling factor for a given portion of deformation cycle
E_{c}	Composite elastic modulus
E_{m}	Elastomer matrix elastic modulus
$E_{\text{c},B=0}$	Zero-field composite elastic modulus
H	Magnetic field strength
W	Work density (generic)
W_{D}	Dissipated work density
W_{L}	Loading work density
W_{mag}	Magnetic work density (generic)
$W_{x,\text{mag}}$	Magnetic work density for a given portion of deformation cycle
W_x	Total work density for a given portion of deformation cycle
η_{s}	Specific loss
μ	Relative permeability
ε	Engineering strain

1. Introduction

Soft functional systems enable new or improved functionalities for robots and machines such as real-time stiffness tuning for reversible adhesion and grasping [1, 2], soft sensing and haptic feedback for medical applications [3, 4], and shape change for multi-modal transport [5]. Magnetically active elastomers are a class of soft functional material that show significant potential for traditional and emerging applications including soft robots and machines [6, 7], soft electronics [8–10], sensors [11, 12], and automotive suspension [13]. These composites are created by incorporating magnetic materials into soft elastomers, which provide magnetic material responses including increased magnetic permeability for the improvement of electronic devices [9, 10, 14] and rapid actuation or shape morphing for robotic systems [1, 15, 16]. MREs are one class of magnetically active materials that can rapidly change mechanical properties such as stiffness and damping in response to a magnetic field [17–20]. In addition, MREs can also change shape and display shape-memory properties [21]. These promising capabilities are linked back to the constituent material properties, the micro- and macrostructure of the components, and how the magnetic field is applied to the materials. These design and control parameters can provide important methods to tune MREs to achieve a desired response.

MREs have traditionally been fabricated as RCs which incorporate micron-scale magnetic particles into soft elastomers such as silicones or polyurethanes [22]. The magneto-mechanical properties of magnetic elastomers are dependent on parameters such as magnetic particle size, shape, and volume fraction, elastomer matrix response, and micro/meso-structure orientation [15, 23]. In addition to RC MREs, researchers have recently begun to use MRFs, [24, 25] which are magnetic fluids that are prepared by mixing magnetic powders in a carrier fluid, as inclusions in elastomers to introduce a combination of strong magnetic response and a low initial modulus. Upon application of a magnetic field, MRFs rapidly realize controllable changes in viscosity and yield stress [26, 27], with their properties controlled through magnetic particle and carrier fluid response, and volume fraction of magnetic filler [28]. The incorporation of MRFs in elastomers provides structure and stability to the fluid, while still achieving a tunable mechanical response. These magnetic FCs have been demonstrated through bulk encapsulation of MRFs in elastomeric solids, [29] through 3D printing millimeter-scale droplets into elastomeric materials, and by creating homogeneous dispersions of micro-droplets in elastomers through high shear mixing [2, 10, 21, 30]. FC MREs have demonstrated excellent stiffness and loss factor control through MR tuning [21], and the processing approaches developed for incorporating MRFs into solid-state structures have lead to unique architectural designs such as HC MREs that incorporate both solid and fluid domains within an elastomer [1, 10]. Understanding how magnetic fluid inclusions affect magneto-mechanical performance, and the interplay between solid and fluid magnetic domains will allow for a data-driven approach for the design of high performing MRE systems.

Significant work has been carried out to understand the adaptive response of MR materials through both experimental trends and constitutive modeling [15, 23, 31, 32]. Modeling and experimental validation of solid-state MR systems have largely been carried out on RC MREs [31, 32],

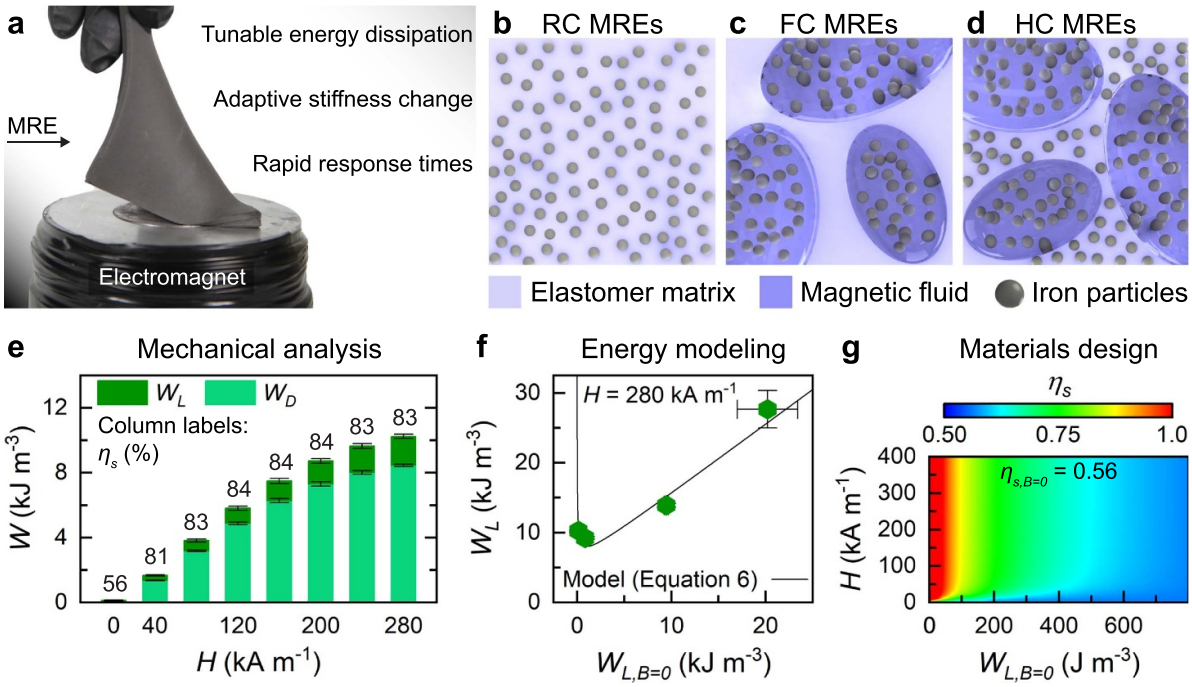

Figure 1. A simplified approach to understanding multi-phase magnetorheological elastomers. (a) Image of a magnetorheological elastomer. (b) Schematics of rigid particle composite (RC), (c) Fluid composite (FC), and (d) Hybrid composite (HC) MREs. (e) Loading and dissipated work densities of an HC MRE ($E_m = 8$ kPa) at various magnetic fields. The percentages above the bars represent specific loss. (f) An energy model predicting the loading work density at $H = 280$ kA m^{-1} for HC MREs as a function of the zero-field loading work density. (g) A design map created from the simplified work model to predict specific loss as a function of field for a range of zero-field loading work densities for a zero-field specific work of 0.56 which corresponds to the HC MRE in e.

whereas newer material architectures such as FC MREs have not been constitutively modeled to understand the differences in performance. The state-of-the-art modeling of RC MREs has generally been carried out through microstructure, continuum, or phenomenological-based approaches [31, 32]. Microstructure-based models often consider the magnetic interaction between particles, ranging from simpler models that consider the magnetic interaction between two adjacent particles [33], to more complex models that consider interactions within and between chain-like particle structures [34]. In contrast, continuum models use a homogeneous approach to determine MRE behavior with early work considering free energy as an explicit function of deformation gradient or magnetic field, or incorporating microstructural effects via implicit magneto-elasticity terms [32, 35]. Phenomenological models have often been used to understand experimentally obtained behavior and are especially useful for the prediction of non-linear MRE response [36, 37]. While the magneto-mechanical response of RC MREs have been extensively studied, there have not yet been phenomenological models to understand the effect of MRF inclusions in solid state MREs, where the known non-linear response of MRF domains may elicit a different response than rigid inclusions [38, 39].

Here we investigate the energy dissipation properties for MREs of diverse, multiphase magnetic material architectures. These MRE's begin with a soft and compliant mechanical response (figure 1(a)), and then rapidly tune their mechanical properties such as energy dissipation and stiffness in the presence of a magnetic field. To investigate the impact of solid and liquid inclusions on MRE performance, the magneto-mechanical properties of three material architectures are experimentally determined. These include RC, FC, and HC MREs (figures 1(b)–(d)) which integrate solid inclusions, fluid inclusions, and a combination of the phases respectively into solid-state elastomers. The magneto-mechanical properties of these architectures are experimentally determined through testing of materials across 4 orders of magnitude of matrix modulus and a range of applied magnetic field strengths. This magneto-mechanical testing provides an understanding of energy applied and dissipated in these systems (figure 1(e)), which we use to create and evaluate an applicable energy model (figure 1(f)). This model, created from magnetic and mechanical energy principles, captures the response of the three material architectures and provides insight into the design of future systems. We show its application towards MRE design by providing design maps for specific loss and elastic modulus as a function of material architecture, zero-field properties, and applied magnetic field strength (figure 1(g)).

2. Experimental methods

2.1. Composite fabrication

To understand the effect of material architecture and zero-field mechanical properties on magneto-mechanical response,

we develop 12 unique material compositions. RC, FC, and HC MREs are each fabricated with four unique silicone elastomer compositions as the matrix material. For simplicity, the composites are labeled by the elastic modulus of the polymer matrix (E_m), where each architecture is fabricated with matrices of $E_m = 8$, 200, 900, and 3000 kPa. The selection of these matrices allows for the experimental characterization, and model validation across 4 orders of magnitude in elastic modulus.

The polymer matrices used in this work are two-part silicone elastomers: Sylgard 184 (Dow Silicones), and Ecoflex 00-30 (Smooth-On). E_m is tuned by either varying the ratio of the two parts of each product line of elastomer, or by combining the two product lines of elastomer. The elastomer precursors are mixed prior to the integration of magnetic inclusions into the composite. The composites with $E_m = 8$ kPa are made by combining a 60:1 ratio of Sylgard 184 base to curing agent in a dual asymmetric centrifugal mixer under vacuum (FlackTek) at 1800 RPM for 100 s. The composites with $E_m = 200$ kPa are fabricated by combining equal parts by weight of Ecoflex 00-30 Part A and Part B. This is then mixed for 270 s at 2000 RPM under a vacuum. The silicone matrix with $E_m = 900$ kPa is made utilizing a combination of Sylgard 184 and Ecoflex 00-30. Ecoflex 00-30 is mixed with equal parts by weight of Part A and Part B for 270 s at 2000 RPM under vacuum. Sylgard 184 is mixed with a 10:1 ratio of base to curing agent at 1800 RPM for 100 s. The two precursors are combined in a 1:1 ratio by weight, and mixed for 270 s at 2000 RPM under vacuum. The composites with $E_m = 3000$ kPa are fabricated with a 10:1 ratio of base to curing agent at 1800 RPM for 100 s under vacuum.

After preparing the precursor, the magnetic inclusions are integrated with the mixtures. RC MREs are created by adding magnetic powder into the prepared elastomer precursor (mean particle diameter: 5 μm, US Research Nanomaterials) at the desired volume fraction of 25%. FC MREs are fabricated by adding a MRF into the elastomer precursor at a loading of 50% by volume. The MRF is created by mixing iron powder into propylene glycol (McMaster-Carr) at a volume fraction of 35%. HC MREs are fabricated by adding 15% iron powder by volume into the elastomer precursor followed by the MRF in a 1:1 ratio of MRF to elastomer precursor by volume. The procedures for fabricating these samples were determined in our previous work [1, 10].

2.2. Magneto-mechanical testing

The magneto-mechanical response is experimentally characterized using a custom-designed magneto-mechanical testing fixture that includes a 500 turn electromagnet wrapped around a magnetic core. Full details and schematics of this testing fixture were discussed in our previous work [1]. Three test specimens for each of the 12 material compositions are fabricated through a mold casting process into cylindrical geometries with diameters of 28.6 mm and thicknesses of 12.5 mm.

Magneto-mechanical testing occurs through a multi-step process that must be used to correct for the attractive magnetic force between the top and bottom compression plates. This process consists of 28 individual tests per sample to experimentally measure the magnetic force of attraction, curve fitting to determine magnetic attraction force as a function of compressive displacement, and then cyclic compression tests for experimental determination of the magneto-mechanical material response with varying field. The process is detailed below: (i) The samples are placed into the magneto-mechanical testing fixture, the balance is zeroed, and the magnetic load is measured with 7 applied magnetic fields between $H = 40$–280 kA m^{-1}. This is carried out at 4 static displacements of 0, 0.5, 1.0, and 1.5 mm. (ii) Next, a power law fit is used to determine the magnetic force as a function of compressive displacement for each sample. (iii) Finally, the full compression tests are run for 8 magnetic fields between $H =$ 0–280 kA m^{-1}, and the magnetic force fit is subtracted from the load *versus* displacement curve of the sample. The compression tests consist of three cycles of compression and return between compressive engineering strains of 0 to 0.1 at rates of 12 mm min^{-1} (0.08 Hz). The composite modulus and work densities are analyzed from the third compression cycle, where the modulus is taken from a linear fit of the loading curve between engineering strains of 0.025 to 0.075.

2.3. Initial magnetic property determination

The magnetic properties needed in this work are relative permeability (μ) and saturation flux density (B_{sat}). The value of μ for the RC and HC MREs are assumed to be the same as the volume fraction of magnetic powder is equivalent at 25% for both architectures. The value used for these samples is $\mu = 2.75 \times 10^{-6}$ H m^{-1} which is taken from the measured value of relative permeability used for the same material composition of HC MREs in previous work where $\mu = \mu_r \mu_0$. [10] The value of μ for FC MREs is estimated from the Maxwell Garnett model (equation (1)) utilizing the total iron powder volume fraction of 17.5% found in these samples. For FC MREs, $\mu = 2.07 \times 10^{-6}$ H m^{-1}

$$\mu_{\text{eff}} = \mu_e + 2\mu_e \frac{\mu_i - \mu_e}{\mu_i + \mu_e - f(\mu_i - \mu_e)}. \tag{1}$$

The saturation flux density for these samples are estimated from experiments run on the same iron powder as used in this work [40]. Here, M_{sat} of the iron powder was determined to be 1.36×10^{-6} A m^{-1}. The magnetization of the composite is then estimated from $M_{sat} = \phi M_{Fe,sat}$. This is converted to B_{sat} through equation (2), where $B_{sat} = 0.783$ T for HC and RC MREs, and $B_{sat} = 0.756$ T for FC MREs

$$B_{sat} = \frac{M_{sat}}{\mu_r - 1}\mu. \tag{2}$$

3. Results and discussion

3.1. Magneto-mechanical energy response

MREs have shown potential for active energy dissipation and damping made possible through large and controllable changes in damping factor (>40%) and loss factor (up to 100% change) [21, 41]. In addition to the MR effect imparted by the magnetic particles within the elastomer, MRFs are known to have tunable viscoelastic character–changing from a liquid to a viscoelastic solid with a storage modulus at least an order of magnitude larger than its loss modulus in response to an applied field [42]. To investigate the magneto-mechanical tuning of multi-phase MREs, samples with diverse matrix moduli (E_m = 8–3000 kPa) are deformed in cyclic compression (figure 2(a)). The energy dissipation properties are calculated through the work densities obtained from the compression cycle, where W_L is the loading work density taken from the area under the loading curve, W_U is the work density obtained from the area under the unloading curve, and the dissipated work density, $W_D = W_L - W_U$, represents the energy dissipated during a single cycle. The specific work (η_s) is the ratio between W_D and W_L, which represents the fraction of loading work density that is dissipated for each cycle and is related to the loss factor, $\tan(\delta)$, or η, for viscoelastic materials [43–45].

The mechanical properties of the elastomer and material architecture of the composite have a large effect on the zero-field response of MREs. Figure 2(b) presents the loading and dissipated work densities in the absence of a magnetic field ($W_{L,B=0}$ and $W_{D,B=0}$) as a function of matrix modulus and material architecture. The zero-field specific loss ($\eta_{s,B=0}$) is shown in the column labels as a percentage. RC MREs generally display a larger $W_{L,B=0}$ when compared to FC or HC MREs of the same E_m. This result is expected as $W_{L,B=0}$ is indicative of the composite modulus (E_c) and previous work has shown that the use of magnetic fluid inclusions do not result in the drastic zero-field stiffness increase observed with many RCs [1, 10].

Figures 2(c)–(e) introduces representative compression curves for RC, FC, and HC MREs (E_m = 200 kPa) under an applied magnetic field of H = 280 kA m^{-1}, which is the highest tested in this work. For this subset of samples, there are clear changes in material response with the application of a magnetic field, and observable differences in both the magnitude of change and the material linearity between the different material architectures. The work densities are analyzed from the stress–strain data, and presented as a function of H in figures 2(f)–(h). The RC MRE (figure 2(f)) begins with a higher specific loss than the FC and HC MREs, requiring the most energy to deform, and dissipating 37% of the input energy prior to the application of a magnetic field. As H is increased to 280 kA m^{-1}, the composite dissipates up to 43% of the energy used to deform the material, but elastically recovers the majority of loading energy throughout all field strengths tested ($\eta_s < 50\%$). The FC MRE (figure 2(g)) begins with a lower $\eta_{s,B=0}$, but achieves a larger change in specific loss ($\Delta\eta_s = 25\%$) as H is increased to 280 kA m^{-1}. The HC MRE (figures 2(h)) demonstrates the largest change in specific loss ($\Delta\eta_s = 27\%$) combined with an $\eta_{s,B=0}$ in between that of the RC and FC MREs. Additionally, this HC MRE presents a unique response that allows for the tuning of η_s from elastically recovering the majority of loading energy ($\eta_s < 50\%$) to dissipating the majority of loading energy ($\eta_s > 50\%$) when increasing the field from 0 to 280 kA m^{-1}. These experiments and analysis indicate a clear difference in response between the three material architectures, which can be understood through magnetic and mechanical energy principles.

3.2. Magneto-mechanical modeling

3.2.1. A simplified energy model. To understand the relationship between magnetic inclusion phase and magneto-mechanical response, and to provide a roadmap for the design of useful MRE technologies, a simple energy model is created. To begin, it is assumed that the field induced work is the sum of two work elements: a material based element, and a magnetic element (equation (3)). The approach of breaking the magneto-mechanical response into mechanical and magnetic elements closely follows similar MRE models based on stress, elastic modulus, and energy density: [1, 32, 46].

$$W = W_{B=0} + W_{mag}. \tag{3}$$

The mechanical work density of a material at zero-field is given by: $W_{B=0} = \int_{\varepsilon_1}^{\varepsilon_2} \sigma\, d\epsilon$, which is the area under the stress–strain curve. The magnetic energy density in a given domain can be determined through: $u = \frac{\mu H^2}{2}$, or equivalently: $u = \frac{B^2}{2\mu}$, where u is the magnetic energy density, μ is the magnetic permeability, and B is the magnetic flux density. The deformation-induced magnetic work density is the work required to induce a change in composite magnetic energy density through a change in strain, $u_{\varepsilon_2} - u_{\varepsilon_1}$:

$$W_{mag} = \left[\frac{B_2^2}{2\mu}\right]_{\varepsilon_2} - \left[\frac{B_1^2}{2\mu}\right]_{\varepsilon_1}. \tag{4}$$

Magnetic materials often have a linear relationship between B and H at low fields, however at high H, the relationship plateaus as B approaches the saturation flux density (B_{sat}). The saturation energy density for a given strain can then be given as $u_{\varepsilon,sat} = \left[\frac{B_{sat}^2}{2\mu}\right]_{\varepsilon}$. We account for saturation by providing a simple limiting relationship between the energy density at constant strain (u_ε) and H:

$$u_\varepsilon = \left[\frac{B_{sat}^2}{2\mu}\left(\frac{H^2}{r\mu^{-2}B_{sat}^2 + H^2}\right)\right]_{\varepsilon}. \tag{5}$$

For simplicity in comparing materials with different permeabilities, equation (5) is written in terms of the independent variable H which is the constant applied field from the

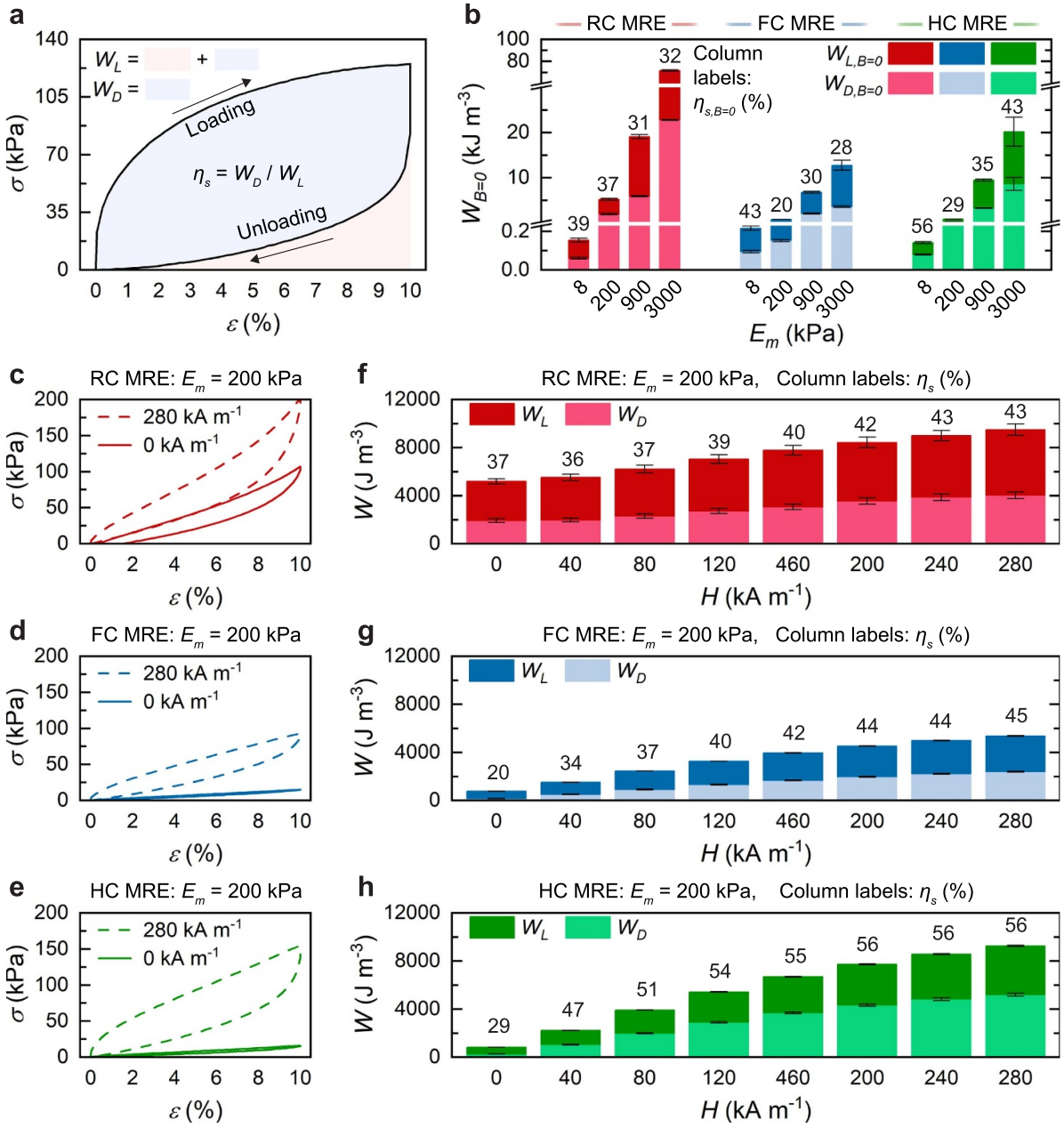

Figure 2. Magnetorheological energy dissipation. (a) Representative cyclic compression curve. (b) Zero-field loading and dissipated work density as a function of matrix modulus. (c)–(e) Cyclic material response for RC, FC, and HC MREs for $E_{\mathrm{m}} = 200$ kPa. (f)–(h) Loading and dissipated work densities for RC, FC, and HC MREs ($E_{\mathrm{m}} = 200$ kPa) as a function of magnetic field strength.

electromagnet, while B_{sat} and μ are assumed constant for a given material at a given strain. The saturation energy density term, $\frac{B_{\mathrm{sat}}^2}{2\mu}$, acts as the limiting value for achievable u_ε, while the right hand term, $\left(\frac{H^2}{r\mu^{-2}B_{\mathrm{sat}}^2+H^2}\right)$, is a fraction that controls the rate at which u_ε approaches $u_{\varepsilon,\mathrm{sat}}$. A unitless rate constant, r, is used to control the onset of the saturation plateau. The relationship between B and H is a controlling factor in the magneto-mechanical limits observed in MREs. By combining the relationships in equations (4) and (5) we achieve an expression for the magnetic work density as a function of applied field (equation (6)) where x is the chosen portion of work to be measured in a given deformation cycle (e.g. loading (L) or dissipated (D)):

$$W_{x,\mathrm{mag}} = C_{W,x}\left[\frac{B_{\mathrm{sat}}^2}{2\mu}\left(\frac{H^2}{r\mu^{-2}B_{\mathrm{sat}}^2+H^2}\right)\right]_{\varepsilon_1}. \tag{6}$$

Here, $C_{W,x}$ is a magneto-mechanical coupling factor which represents the conversion of magnetic energy density prior to deformation to magneto-mechanical work observed during

deformation. In principle, $C_{W,x}$ should be equivalent to the relative change in magnetic energy density: $\frac{u_{\varepsilon_1 2}-u_{\varepsilon_1}}{u_{\varepsilon_1}}$ where u_{ε_1} is given by $\left[\frac{B_{\text{sat}}^2}{2\mu}\left(\frac{H^2}{r\mu^{-2}B_{\text{sat}}^2+H^2}\right)\right]_{\varepsilon_1}$. By combining equations (3) and (6), a model that represents work density of the MRE at a given field is obtained:

$$W_x = C_{W,x}\left[\frac{B_{\text{sat}}^2}{2\mu}\left(\frac{H^2}{r\mu^{-2}B_{\text{sat}}^2+H^2}\right)\right]_{\varepsilon_1} + W_{x,B=0}. \quad (7)$$

The left hand term of equation (7) represents the active magnetic contribution to observed work, while the right hand side represents the zero-field mechanical contribution. This equation provides a mechanism to quantify the effect of material architecture and zero-field properties on active MRE response through a magneto-mechanical coupling factor ($C_{W,x}$).

3.2.2. Understanding the response of multi-phase MREs. The model is first used to understand the material behavior by fitting to the magnetic components of the loading work density ($W_{\text{L,mag}}$) and dissipated work density ($W_{\text{D,mag}}$). $W_{\text{L,mag}}$ and $W_{\text{D,mag}}$ are experimentally determined by subtracting the zero-field work density from the work density at field H. Applying the model to the experimental data requires known initial values of μ and B_{sat}, as well as the independent variable H. The values of μ and B_{sat} are determined using the known values of previously measured composites and the volume fraction of magnetic inclusions as described in the Methods section. The values used in this work are $\mu = 2.07\times10^{-6}$ H m^{-1} and $B_{\text{sat}} = 0.756$ T for FC MREs, and $\mu = 2.75\times10^{-6}$ H m^{-1} and $B_{\text{sat}} = 0.783$ T for both the RC and HC MREs. The differences in properties between the FC MREs and the other architectures are due to the different magnetic particle volume fractions between samples. While, RC and HC MREs have an identical volume fraction of $\phi = 25\%$, FC MREs contain magnetic particle volume fractions of $\phi = 17.5\%$ with another 32.5% of the inclusion volume occupied by the non-magnetic carrier fluid. The lower magnetic content is the result of processing challenges due to phase separation of magnetic fluids at high loading [1]. After determining the necessary material properties, the model is fit to the measured values of $W_{\text{L,mag}}$ and $W_{\text{D,mag}}$ respectively using equation (6) such that:

$$W_{\text{L,mag}} = C_{W,\text{L}}\left[\frac{B_{\text{sat}}^2}{2\mu}\left(\frac{H^2}{r\mu^{-2}B_{\text{sat}}^2+H^2}\right)\right]_{\varepsilon_1} \quad (8)$$

and

$$W_{\text{D,mag}} = C_{W,\text{D}}\left[\frac{B_{\text{sat}}^2}{2\mu}\left(\frac{H^2}{r\mu^{-2}B_{\text{sat}}^2+H^2}\right)\right]_{\varepsilon_1}. \quad (9)$$

Figure 3 shows the experimental and modeled response for RC, FC, and HC MREs where the matrix modulus (E_{m}) is varied between 8 and 3000 kPa. The model statistics (R-squared (R^2) and root mean squared error percentages (*RMSEP*) for each model in this work can be found in the section S1 of the supplementary information. Figures 3(a)–(c) presents the fitted plots for the loading magnetic work density, while figures 3(d)–(f) presents the fitted plots for the dissipated magnetic work density. r dictates the rate at which B approaches B_{sat}, and is held constant at $r = 0.21$ for all samples, which reasonably fits the measured response for each material architecture. The data is then fit by varying only one fitting parameter ($C_{W,x}$) for each work term, which captures the conversion across all field strengths for a single microstructure and E_{m}. All of the materials tested in this work show an increase in both $W_{\text{L,mag}}$ and $W_{\text{D,mag}}$ as a function of H, and each material architecture demonstrates an inverse relationship between magnetic work density and E_{m} for a given field, with the largest absolute increases in $W_{\text{L,mag}}$ and $W_{\text{D,mag}}$ occurring at $E_{\text{m}} = 8$ kPa, and the smallest changes occurring in the most rigid elastomers. Between material architectures, HC MREs generally show the largest increase in both $W_{\text{L,mag}}$ and $W_{\text{D,mag}}$ for a given E_{m}, however the RC MRE with $E_{\text{m}} = 8$ kPa demonstrates the largest change in magnetic work density of the samples tested. The magnetic work densities as a function of H demonstrate clear differences both within a single material architecture for changing E_{m} and between material architectures for a constant E_{m}. As the modeled results are obtained while varying only the magneto-mechanical coupling factor, this indicates that $C_{W,x}$ may have a strong dependence on both the zero-field mechanical properties and architecture of the sample.

3.3. Work as a foundation for MRE properties

3.3.1. Specific loss. Understanding the relationship between work density and applied field allows for the prediction of the achievable mechanical properties important for MRE technologies. Materials can be characterized by several properties for damping and energy dissipation applications, including total dissipated energy, loss factor, and loss modulus for quasi-static and dynamic applications [45, 47, 48]. To show the extension of the model for these applications, the magneto-mechanical coupling factors obtained in section 3.2.2 are used to determine specific loss. This is accomplished by combining equations (7)–(9) to obtain η_{s}, which is simply the ratio of dissipated to loading energy:

$$\eta_{\text{s}} = \frac{C_{W,\text{D}}\left[\frac{B_{\text{sat}}^2}{2\mu}\left(\frac{H^2}{r\mu^{-2}B_{\text{sat}}^2+H^2}\right)\right]_{\varepsilon_1} + W_{\text{D},B=0}}{C_{W,\text{L}}\left[\frac{B_{\text{sat}}^2}{2\mu}\left(\frac{H^2}{r\mu^{-2}B_{\text{sat}}^2+H^2}\right)\right]_{\varepsilon_1} + W_{\text{L},B=0}}. \quad (10)$$

Figures 3(g)–(i) shows the measured and modeled specific loss for each of the material architectures. For materials with low E_{m}, η_{s} is observed to experience rapid growth at low magnetic fields up to $H = \simeq 40$ kA m^{-1} followed by a plateau value. The data suggests that as E_{m} increases, the materials require a higher magnetic field to reach the η_{s} plateau value. The determination of specific loss provides opportunities for a more in depth understanding of quasi-static dissipation and

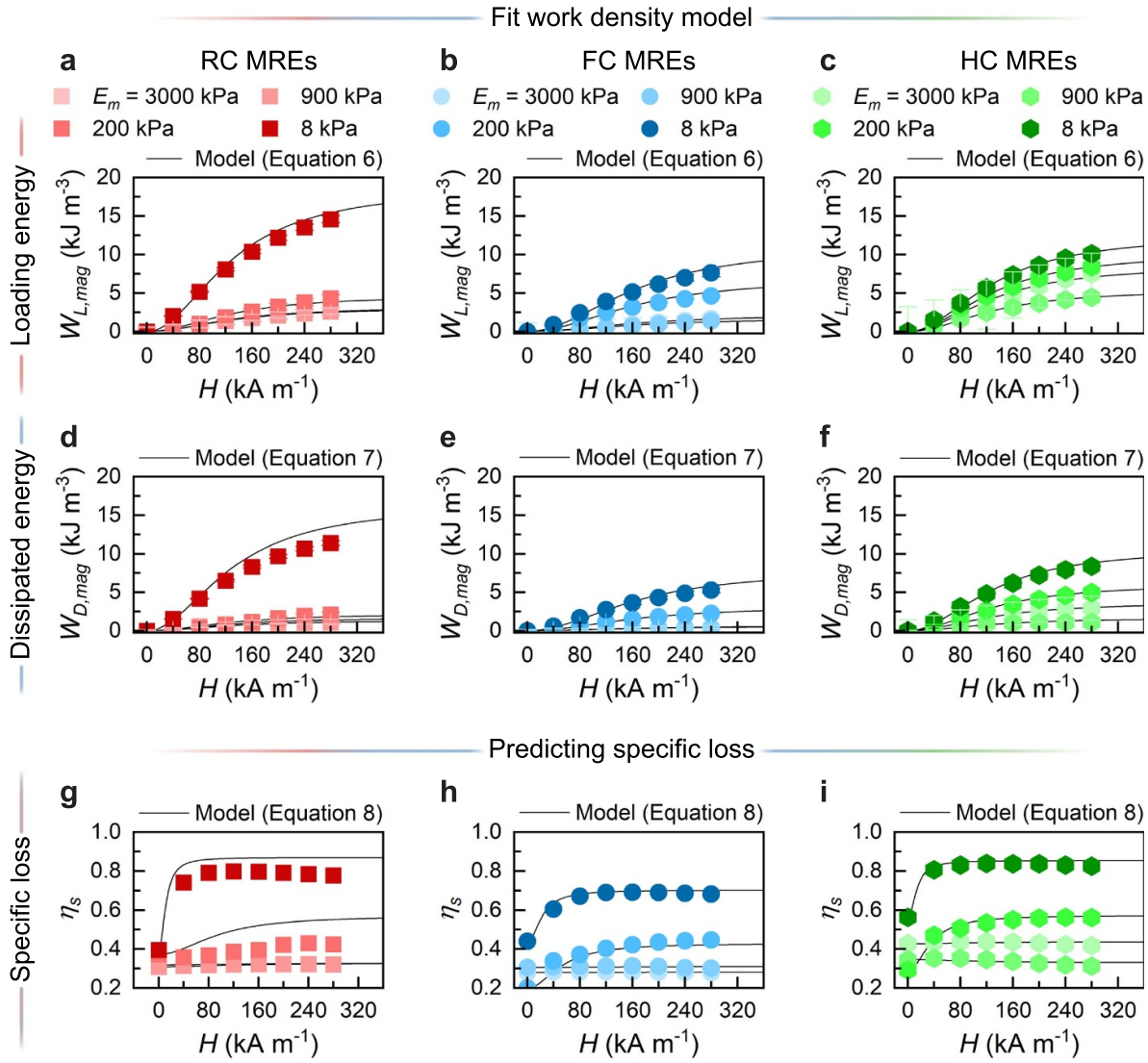

Figure 3. Magneto-mechanical modeling. (a)–(c) Application of work density model to the loading energy of RC, FC, and HC MREs with a range of E_m. (d)–(f) Application of work density model to the dissipated energy for each material architecture. (g)–(i) Extension of the magneto-mechanical model to specific loss based on the parameters determined in (a)–(f). Model statistics can be found in table S1.

dynamic damping properties, as η_s is related to $\tan(\delta)$ and loss modulus [45, 48].

3.3.2. Elastic modulus. Our model can estimate the elastic modulus as a function of applied field through a linear elastic relationship. For a linear elastic solid, the elastic modulus can be related to work through $E = \frac{2W_L}{\varepsilon_2^2}$. This relationship allows for the estimation of our zero-field composite modulus $E_{c,B=0}$ through:

$$E_{c,B=0} = \frac{2W_{L,B=0}}{\varepsilon_2^2}. \tag{11}$$

For the tests carried out in this work, the maximum strain is $\varepsilon_2 = 0.1$, which upon substitution into equation (11) shows that elastic modulus can be approximated by $E_c = 200W_L$. Additionally, as the modulus is linearly proportional to work, equations (7) and (11) can be used to obtain:

$$E_{c,mag} = C_E \left[\frac{B_{sat}^2}{2\mu} \left(\frac{H^2}{r\mu^{-2}B_{sat}^2 + H^2} \right) \right]_{\varepsilon_1} \tag{12}$$

where,

$$C_E = \frac{2C_{W,L}}{\varepsilon_2^2} \tag{13}$$

Here, C_E is used for the conversion between the magneto-mechanical work density of loading and elastic modulus. The conversion allows for direct fitting of the magnetic contribution to the composite elastic modulus $E_{c,mag}$ from experimental data, and will be useful in the creation of the stiffness tuning design maps featured later in this work. Figures 4(a)–(c)

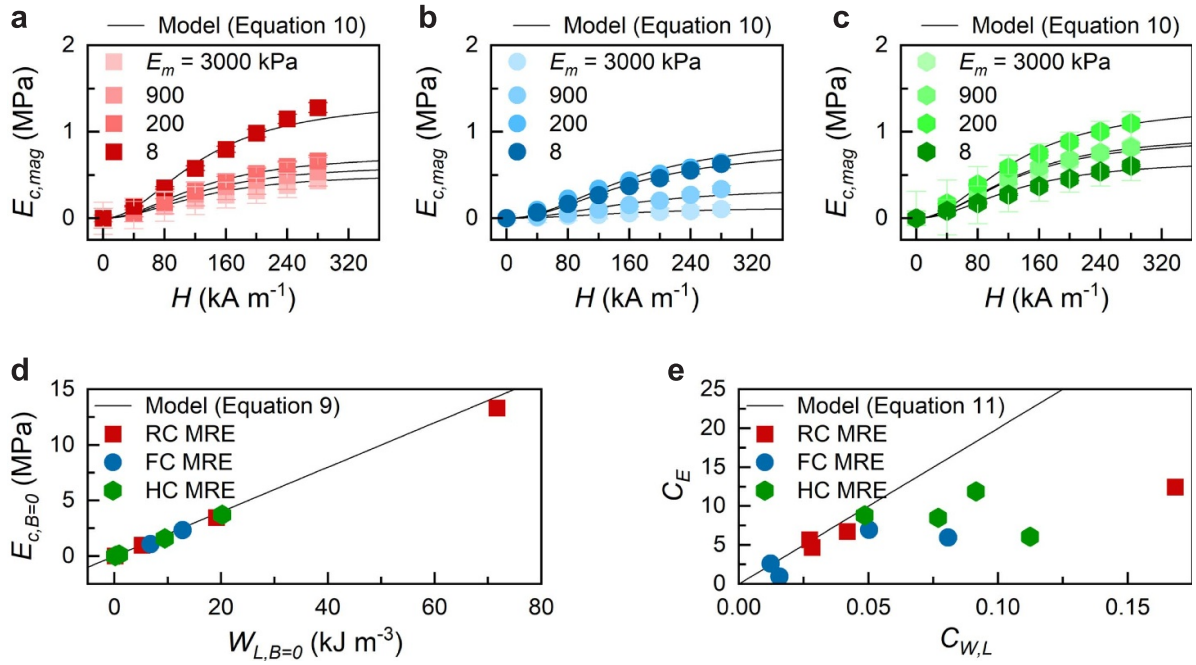

Figure 4. Work model to modulus. (a)–(c) Application of work model to elastic modulus of RC, FC, and HC MREs with a range of E_m. (d) Zero-field modulus as a function of zero-field loading work density. (e) Relationship between the magneto-mechanical coupling factors for modulus and loading work density. Model statistics can be found in table S2.

shows $E_{c,mag}$ as a function of magnetic field. Equation (12) is fit to the experimental data using the same rate constant, $r = 0.21$ as for the previous work density fits, with C_E as the fitting parameter. To qualify the ability of a linear elastic approximation to capture the measured zero-field response, $E_{c,B=0}$ is plotted as a function of W_L (figure 4(d)) along with the approximation from equation (11). The data is captured with a linear fit of slope $\frac{2W_L}{\varepsilon_2^2} = 200$ as predicted by the linear elastic approximation. To allow for conversion between the active work density and stiffness tuning properties, the relationship between C_E and $C_{W,L}$ is explored in figure 4(e). Here, the magneto-mechanical coupling factors for elastic modulus and loading work density are shown along with the linear elastic approximation (equation (13)). The approximation allows for a simple prediction of elastic modulus with respect to magnetic response, capturing the trend at low values of the magneto-mechanical coupling factors. However, C_E is over-predicted for materials with high $C_{W,L}$, which correspond to the composites with low $E_{c,B=0}$. The over-prediction can be attributed to the increased magneto-mechanical response of the low zero-field stiffness composites, which show the highest changes in both work density of loading and dissipated work density (figures 2 and 3), and show more non-linearity to the mechanical response. One approach to improving the linear elastic approximation may be to analyze the composite modulus using the unloading portion of the curve, which captures the elastic recovery without dissipative losses. Initial analysis using this method can be found in figure S1.

3.4. Designing MREs

3.4.1. Magneto-mechanical coupling. Understanding strategies to control the magneto-mechanical coupling factor ($C_{W,x}$) will allow for useful design strategies. $C_{W,x}$ demonstrates a dependence on material architecture, with an observed differences dependent on E_m, and the initial properties: $W_{L,B=0}$ and $W_{D,B=0}$. To understand the relationship between the magneto-mechanical coupling factor and the zero-field response, $C_{W,L}$ and $C_{W,D}$ are plotted as a function of $W_L, B = 0$ and $W_D, B = 0$ respectively (figures 5(a) and (b)).

The magneto-mechanical coupling factors for all architectures display a decrease as the zero-field work densities are increased prior to an apparent plateau value. While the decrease is present for all architectures, the relative trends for $C_{W,L}$ and $C_{W,D}$ of RC, FC, and HC MREs appear to diverge as $W_{L,B=0} > 5$ kJ m^{-3}, and as $W_{D,B=0} > 2.5$ kJ m^{-3} indicating a difference in magnetic energy density response between the material architectures. We hypothesize that the difference in coupling factors are the result of the nonlinear dependence of magnetization on the stiffness of the surrounding matrix. The dependence of magnetization (and therefore B) as a function of H is dependent on the medium surrounding the embedded magnetic particles, with softer mediums allowing for restructuring of the magnetic particles in response to a magnetic field, which can lead to larger initial permeabilities in the direction of the field [49]. The trends between material architectures may also be the result of differences in demagnetization and

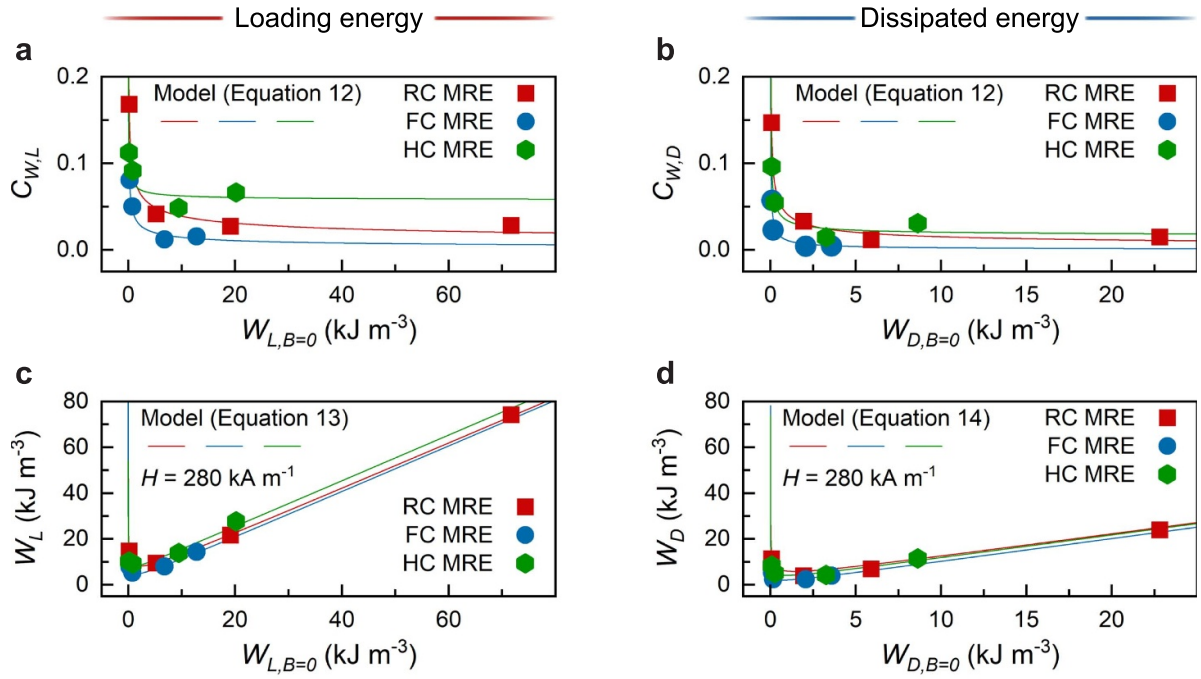

Figure 5. Magneto-mechanical coupling. (a), (b) Influence of zero-field mechanical response on the magneto-mechanical coupling factor for loading and dissipation. (c), (d) Application of model using predicted magneto-mechanical coupling factor values for the work density of loading and dissipation. Model statistics can be found in table S3.

permeability arising from larger microstructural anisotropy occurring during magnetization in the magnetic fluid domains. For all samples, a low $W_{\mathrm{L},B=0}$ is indicative of low stiffness, and the magnetic inclusions are able to orient in the direction of the applied field, changing the local structure from discrete particles to more chain-like configurations [50]. As $W_{\mathrm{L},B=0}$ increases, the ability of the inclusions to re-orient is constrained. For RC MREs, the material approaches a critical stiffness where the particles are constrained from motion, resulting in a plateau for conversion. For FC MREs, the relationship is more complex. The addition of discrete fluid inclusions may allow for a higher degree of alignment at high stiffness, resulting in a higher conversion plateau. HC MREs, which contain magnetic particles in both the matrix and fluid phase, offer the advantage of allowing for alignment in the fluid domain while having a higher permeability matrix phase because of the integrated particles. The nonlinear relationship between permeability and deformation especially for samples with low $E_{\mathrm{c},B=0}$ or the inclusion of fluid domains represents a unique challenge for accurately quantifying a change in magnetic energy density. However, an understanding of the relationship between conversion and initial work density allows for the prediction of magneto-mechanical response for given zero-field material properties. A prediction of the trend using a two parameter function is approximated by:

$$C_{W,x} = W_{x,B=0}^{A_x} + B_x. \tag{14}$$

Here, A_x is a parameter that determines rate of decrease of the magneto-mechanical coupling factor ($A_x < 1$), and B_x determines the plateau value. Equation (14) can be combined with equations (8) and (9) to predict the work density response across a range of initial material properties through the following equations:

$$W_{\mathrm{L}} = \left(W_{\mathrm{L},B=0}^{A_{\mathrm{L}}} + B_{\mathrm{L}}\right)\left[\frac{B_{\mathrm{sat}}^2}{2\mu}\left(\frac{H^2}{r\mu^{-2}B_{\mathrm{sat}}^2 + H^2}\right)\right]_{\varepsilon_1} + W_{\mathrm{L},B=0} \tag{15}$$

and

$$W_{\mathrm{D}} = \left(W_{\mathrm{D},B=0}^{A_{\mathrm{D}}} + B_{\mathrm{D}}\right)\left[\frac{B_{\mathrm{sat}}^2}{2\mu}\left(\frac{H^2}{r\mu^{-2}B_{\mathrm{sat}}^2 + H^2}\right)\right]_{\varepsilon_1} + W_{\mathrm{D},B=0}. \tag{16}$$

The measured and predicted values of the W_{L} and W_{D} for $H = 280$ kA m^{-1} are shown in figure 5(c) and (d). Soft materials with low zero-field work densities display a highly tunable mechanical response, owing to the magnetic contribution to the work density becoming much greater than the zero-field value. However, as the zero-field work densities increase, active material response for W_{L} and W_{D} approach the same values as the zero-field response $W_{\mathrm{L},B=0}$ and $W_{\mathrm{D},B=0}$, indicating a negligible relative change in work density.

3.5. MRE design

By understanding the relationship between the magneto-mechanical coupling factors and zero-field mechanical

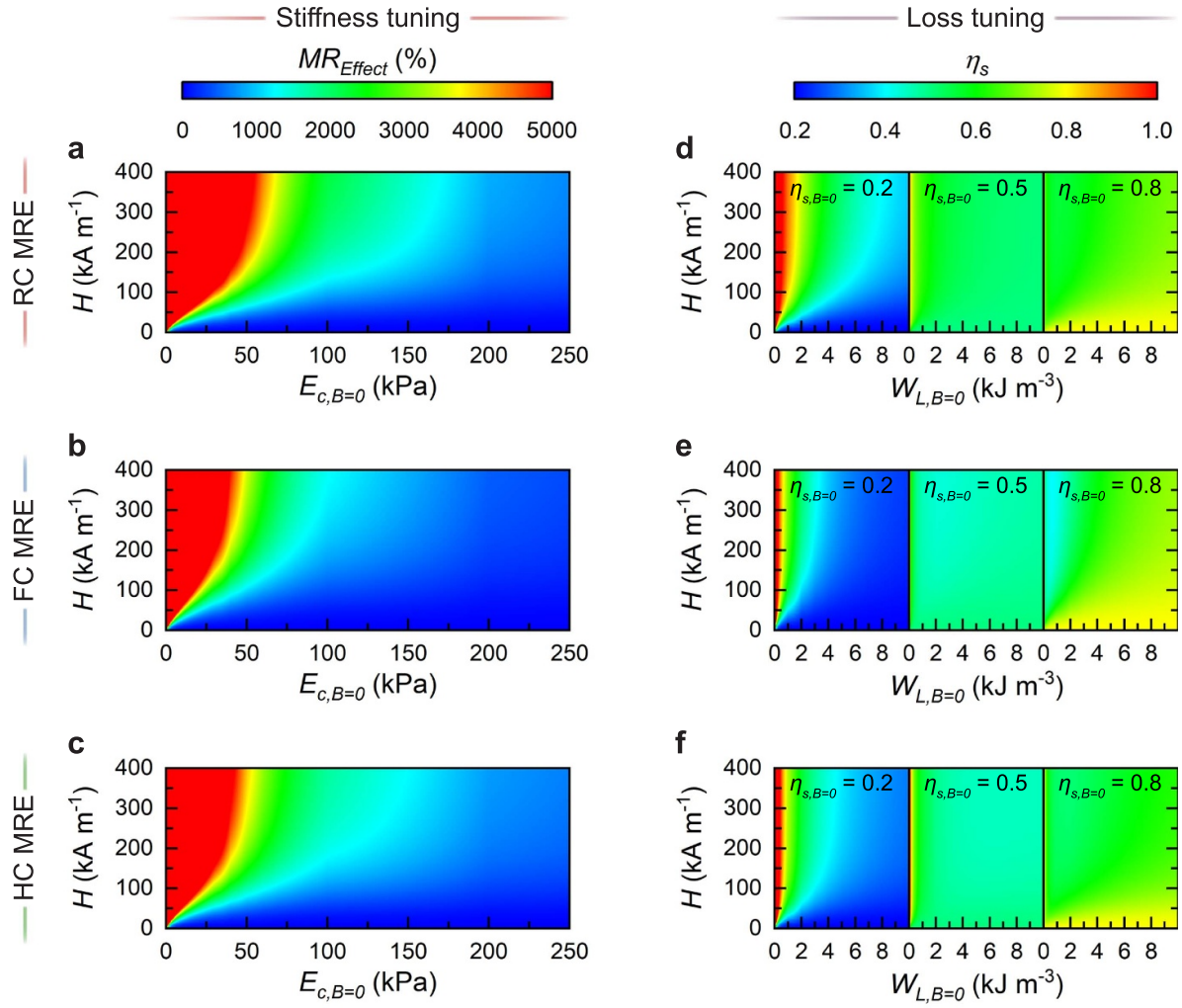

Figure 6. Design maps. Application of magneto-mechanical model to RC, FC, and HC MREs as a function of zero-field properties and applied field. (a)–(c) Modulus. (d)–(f) Specific loss.

response, we can create design maps relating the initial material properties for each architecture to their tunable mechanical response. The stiffness tuning response of MREs is often reported by the relative change in stiffness also known as the MR effect, where $E_{c,B>0}$ is the composite modulus at a given applied field:

$$MR_{\text{Effect}} = \frac{E_{c,B>0} - E_{c,B=0}}{E_{c,B=0}} \times 100\%. \tag{17}$$

The MR effect can be estimated with our work model by substituting equations (12), (14) and (17) to obtain:

$$MR_{\text{Effect}} = \frac{\left(W_{L,B=0}^{A_L} + B_L\right)\left[\frac{B_{sat}^2}{2\mu}\left(\frac{H^2}{r\mu^{-2}B_{sat}^2+H^2}\right)\right]_{\varepsilon_1}}{W_{L,B=0}} \times 100\%. \tag{18}$$

This equation is used to create the design maps for RC, FC, and HC MREs shown in figures 6(a)–(c). The design maps show that the MR Effect is greatly dependent on the zero-field modulus of the samples as well as the applied magnetic field. RC and HC MREs allow for greater stiffness tuning at higher $E_{c,B=0}$, where these material architectures can achieve greater than a 50× increase in modulus (shown in red) at $E_{c,B=0} <$ 50 kPa and maintain greater than a 20× increase in modulus (shown in green) for $E_{c,B=0} <$ 150 kPa. These materials are also able to maintain up to 200% changes in composite modulus at $E_{c,B=0} <$ 1 MPa (figure S2). FC MREs require a softer zero-field modulus for high stiffness change, likely owing to their lower B_{sat} and μ due to a lower volume fraction of magnetic inclusions.

In addition to MR_{Effect}, a design map for specific loss is created by substituting equations (10) and (14), to obtain equation (19), where $W_{D,B=0} = \eta_{s,B=0} W_{L,B=0}$ by the definition of specific loss. This equation allows for the creation of design maps as a function of $W_{L,B=0}$ for a given zero-field specific loss:

$$\eta_s = \frac{\left(\left(\eta_{s,B=0}W_{L,B=0}\right)^{A_D} + B_D\right)\left[\frac{B_{sat}^2}{2\mu}\left(\frac{H^2}{r\mu^{-2}B_{sat}^2+H^2}\right)\right]_{\varepsilon_1} + \eta_{s,B=0}W_{L,B=0}}{\left(W_{L,B=0}^{A_L} + B_L\right)\left[\frac{B_{sat}^2}{2\mu}\left(\frac{H^2}{r\mu^{-2}B_{sat}^2+H^2}\right)\right]_{\varepsilon_1} + W_{L,B=0}}. \tag{19}$$

The design maps can be found in figures 6(d)–(f). For $\eta_{s,B=0} = 0.2$, the largest increase in specific loss occurs at

$W_{L,B=0} < 1$ kJ m^{-3} approaching (or exceeding) values of 1 (shown in red). The values where $\eta_s \geqslant 1$ indicate larger energy dissipation than the applied work of loading, and are a current limitation of the equation (14) fits to the magneto-mechanical coupling factors for sufficiently soft materials. While improved modeling of the relationship between magneto-mechanical coupling and zero-field response will improve these design maps, the model captures the response across a wide range of zero-field work densities and zero-field specific loss. RC MREs appear to realize the largest tuning potential in η_s for a given $W_{L,B=0}$ followed by HC and FC MREs. Interestingly, as $\eta_{s,B=0}$ increases to 0.5 and 0.8, the model predicts a decrease in specific loss to $\eta_s < \eta_{s,B=0}$ as the field strength is increased, with the largest decreases predicted for low values of $W_{L,B=0}$. This effect is similar to those observed in previous work on FC MREs, where the low frequency response showed an increase in loss factor from 0.15 to 0.4 as field was increased, yet at high frequencies, the loss factor began at 0.7 and dropped to 0.3 upon application of a 1 T magnetic field [21].

4. Conclusion

This work demonstrates a simplified energy approach for the determination of the magneto-mechanical response of MREs tested under low frequency compression cycles. The model can be utilized to understand the magneto-mechanical work density for loading and dissipation scenarios to predict magneto-mechanical response as a function of magnetic field strength and the zero-field mechanical properties across a range of material architectures. We utilize a magneto-mechanical coupling factor to fit experimental data and find this factor generally decreases with an increase in E_m, showing that softer materials tend to show more enhanced MRE effects. These work density models demonstrate strong fits to the experimental results ($0.915 \leqslant R^2 \leqslant 0.996$) and accurate predictions of experimental data ($3.91\% \leqslant RMSEP \leqslant 21.83\%$). The extension of these models to the specific loss and composite modulus are shown to capture the magneto-mechanical response for a broad collection of MRE architectures and zero-field properties ($0.48\% \leqslant RMSEP \leqslant 25.08\%$). The relationship between magneto-mechanical coupling factor and the zero-field mechanical response is then estimated by using a two parameter fitting function ($0.826 \leqslant R^2 \leqslant 0.994$, $7.08\% \leqslant RMSEP \leqslant 41.48\%$) that provides a foundational understanding of the link between materials design considerations and magneto-mechanical response. This allows for the creation of design maps that predict the magneto-mechanical properties with respect to material architecture, zero-field properties, and applied magnetic field strength.

Data availability statement

The data that support the findings of this study are available upon reasonable request from the authors.

Acknowledgments

We acknowledge support from the Office of Naval Research Young Investigator Program (YIP) (N000142112699).

Author contributions

E J B, E T W, N L, and M D B designed research; E J B and E T W performed research; E J B, E T W, N L, and M D B analyzed data; E J B, E T W, N L, and M D B wrote the paper.

Conflict of interest

There are no conflicts to declare.

ORCID iDs

Edward J Barron III https://orcid.org/0000-0002-1091-1217
Ella T Williams https://orcid.org/0009-0008-3160-9333
Nathan Lazarus https://orcid.org/0000-0001-9743-9682
Michael D Bartlett https://orcid.org/0000-0002-7391-5135

References

[1] Barron E J, Williams E T, Tutika R, Lazarus N and Bartlett M D 2023 A unified understanding of magnetorheological elastomers for rapid and extreme stiffness tuning *RSC Appl. Polym.* **1** 315–24
[2] Testa P, Chappuis Bıt, Kistler S, Style R W, Heyderman L J and Dufresne E R 2020 Switchable adhesion of soft composites induced by a magnetic field *Soft Matter* **16** 5806–11
[3] Gerald A and Russo S 2024 Soft sensing and haptics for medical procedures *Nat. Rev. Mater.* **9** 86–88
[4] Van Lewen D, Wang C, Chan Lee H, Devaiah A, Upadhyay U and Russo S 2024 Capacitive origami sensing modules for measuring force in a neurosurgical, soft robotic retractor *2024 IEEE Int. Conf. on Robotics and Automation (ICRA)* (IEEE) pp 5302–8
[5] Hwang D, Barron E J, Tahidul Haque A B M and Bartlett M D 2022 Shape morphing mechanical metamaterials through reversible plasticity *Sci. Robot.* **7** eabg2171
[6] Bira N, Dhagat P and Davidson J R 2020 A review of magnetic elastomers and their role in soft robotics *Front. Robot. AI* **7** 588391
[7] Style R W, Tutika R, Young Kim J and Bartlett M D 2021 Solid–liquid composites for soft multifunctional materials *Adv. Funct. Mater.* **31** 2005804
[8] Ramachandran V, Bartlett M D, Wissman J and Majidi C 2016 Elastic instabilities of a ferroelastomer beam for soft reconfigurable electronics *Extreme Mech. Lett.* **9** 282–90
[9] Lazarus N, Meyer C D, Bedair S S, Slipher G A and Kierzewski I M 2015 Magnetic elastomers for stretchable inductors *ACS Appl. Mater. Int.* **7** 10080–4
[10] Barron E J, Peterson R S, Lazarus N and Bartlett M D 2020 Mechanically cloaked multiphase magnetic elastomer soft composites for wearable wireless power transfer *ACS Appl. Mater. Interfaces* **12** 50909–17

[11] Mateev V and Marinova I 2021 Magnetic elastomer sensor for dynamic torque and speed measurements *Electronics* **10** 309

[12] Hellebrekers T, Kroemer O and Majidi C 2019 Soft magnetic skin for continuous deformation sensing *Adv. Intell. Syst.* **1** 1900025

[13] Ginder J M, Nichols M E, Elie L D and Tardiff J L 1999 Magnetorheological elastomers: properties and applications *Proc. SPIE* **3675** 131–8

[14] Bury E, Thiagarajan S, Lazarus N and Koh A 2022 Ferrofluid high internal phase emulsion polymer foams for soft, magnetic materials *J. Magn. Magn. Mater.* **563** 169921

[15] Ennis J M, Thatcher H G, Calascione T M, Jimmy L, Fischer N A, Ziemann S J, Höft T and Nelson-Cheeseman B B 2023 Effects of infill orientation and percentage on the magnetoactive properties of 3D printed magnetic elastomer structures *Addit. Manufact. Lett.* **4** 100109

[16] Cheng Y, Hoe Chan K, Wang X-Q, Ding T, Tongtao Li, Zhang C, Wanheng L, Zhou Y and Ghim Wei H 2021 A fast autonomous healing magnetic elastomer for instantly recoverable, modularly programmable and thermorecyclable soft robots *Adv. Funct. Mater.* **31** 2101825

[17] Jolly M R, David Carlson J, Muñoz B C and Bullions T A 1996 The magnetoviscoelastic response of elastomer composites consisting of ferrous particles embedded in a polymer matrix *J. Intell. Mater. Syst. Struct.* **7** 613–22

[18] Moreno M A, Jorge Gonzalez-Rico M L L-D, Arias A and Garcia-Gonzalez D 2021 New experimental insights into magneto-mechanical rate dependences of magnetorheological elastomers *Composites B* **224** 109148

[19] Zając P, Kaleta J, Lewandowski D and Gasperowicz A 2010 Isotropic magnetorheological elastomers with thermoplastic matrices: structure, damping properties and testing *Smart Mater. Struct.* **19** 045014

[20] Raa Khimi S and Pickering K L 2015 Comparison of dynamic properties of magnetorheological elastomers with existing antivibration rubbers *Composites B* **83** 175–83

[21] Testa P, Style R W, Cui J, Donnelly C, Borisova E, Derlet P M, Dufresne E R and Heyderman L J 2019 Magnetically addressable shape-memory and stiffening in a composite elastomer *Adv. Mater.* **31** 1900561

[22] Bastola A K and Hossain M 2020 A review on magneto-mechanical characterizations of magnetorheological elastomers *Composites B* **200** 108348

[23] Calascione T M, Fischer N A, Lee T J, Thatcher H G and Nelson-Cheeseman B B 2021 Controlling magnetic properties of 3D-printed magnetic elastomer structures via fused deposition modeling *AIP Adv.* **11** 025223

[24] Soon Kang S, Choi K, Nam J-D and Jin Choi H 2020 Magnetorheological elastomers: fabrication, characteristics and applications *Materials* **13** 4597

[25] Hana Ahmad Khairi M, Yasser Abd Fatah A, Saiful Amri Mazlan U U, Azmah Nordin N, Intan Nik Ismail N, Bok Choi S and Aishah Abdul Aziz S 2019 Enhancement of particle alignment using silicone oil plasticizer and its effects on the field-dependent properties of magnetorheological elastomers *Int. J. Mol. Sci.* **20** 4085

[26] Ashtiani M, Hashemabadi S H and Ghaffari A 2015 A review on the magnetorheological fluid preparation and stabilization *J. Magn. Magn. Mater.* **374** 716–30

[27] Bossis G, Lacis S, Meunier A and Volkova O 2002 Magnetorheological fluids *J. Magn. Magn. Mater.* **252** 224–8

[28] Thiagarajan S and Koh A S 2021 Simultaneous thermo-magnetorheological response of magnetorheological fluids: effect of concentration and composition *IEEE Trans. Magn.* **57** 1–8

[29] Bastola A K, Li L and Paudel M 2018 A hybrid magnetorheological elastomer developed by encapsulation of magnetorheological fluid *J. Mater. Sci.* **53** 7004–16

[30] Bastola A K, Hoang V T and Li L 2017 A novel hybrid magnetorheological elastomer developed by 3D printing *Mater. Des.* **114** 391–7

[31] Asun Cantera M, Behrooz M, Gibson R F and Gordaninejad F 2017 Modeling of magneto-mechanical response of magnetorheological elastomers (MRE) and MRE-based systems: a review *Smart Mater. Struct.* **26** 023001

[32] Saber A and Sedaghati R 2023 The modeling of magnetorheological elastomers: a state-of-the-art review *Adv. Eng. Mater.* **25** 2300182

[33] Shen Y, Farid Golnaraghi M and Rz Heppler G 2004 Experimental research and modeling of magnetorheological elastomers *J. Intell. Mater. Syst. Struct.* **15** 27–35

[34] Gao W, Guo Z and Yang Y 2021 Effect of intensity of orientational magnetic field on steady shear behavior of magnetorheological elastomers *AIP Adv.* **11** 055102

[35] Bustamante R and Rajagopal K R3326341 2015 Implicit constitutive relations for nonlinear magnetoelastic bodies *Proc. R. Soc.* A **471** 20140959

[36] Xin F-L, Bai X-X and Qian Li-J 2016 Modeling and experimental verification of frequency-, amplitude- and magneto-dependent viscoelasticity of magnetorheological elastomers *Smart Mater. Struct.* **25** 105002

[37] Nadzharyan T A, Kostrov S A, Stepanov G V and Yu Kramarenko E 2018 Fractional rheological models of dynamic mechanical behavior of magnetoactive elastomers in magnetic fields *Polymer* **142** 316–29

[38] Salloom M Y 2022 Modeling behavior of magnetorheological fluids *Encyclopedia Smart Mater.* **5** 224–36

[39] Pei P and Peng Y 2022 Constitutive modeling of magnetorheological fluids: a review *J. Magn. Magn. Mater.* **550** 169076

[40] Kiarie W M, Barron E J, Baghel A P S, Nlebedim I C, Bartlett M D and Jiles D C 2020 Modeling of magnetic properties of magnetorheological elastomers using JA hysteresis model *IEEE Trans. Magn.* **57** 1–5

[41] Syam T M I and Muthalif A G A 2020 Hysteresis behaviour of different magnetorheological elastomer models: modelling and simulation *Vibroengineering Procedia* **31** 7–14

[42] De Vicente J, Klingenberg D J and Hidalgo-Alvarez R 2011 Magnetorheological fluids: a review *Soft matter* **7** 3701–10

[43] Chaves M C, Castro D and David Pertuz Comas A 2024 Uniaxial fatigue study of a natural-based bio-composite material reinforced with fique natural fibers *Fracture Structural Integrity/Frattura ed Integrità Strutturale* **68**

[44] Zhang D, Scarpa F, Yanhong M, Boba K, Hong J and Hongwei L 2013 Compression mechanics of nickel-based superalloy metal rubber *Mater. Sci. Eng.* A **580** 305–12

[45] Liu S, Aiqun Li, Siyuan H and Xuan P 2015 Cyclic compression behavior and energy dissipation of aluminum foam–polyurethane interpenetrating phase composites *Composites A* **78** 35–41

[46] Varga Z, Filipcsei G and Zrínyi M 2006 Magnetic field sensitive functional elastomers with tuneable elastic modulus *Polymer* **47** 227–33

[47] Kukla M, Talaśka K and Malujda I 2019 Damping in magnetorheological elastomers under compressive stress

MATEC Web of Conferences vol 254 (EDP Sciences) p 06002

[48] Manin L, Lorenzon C and Liang X 2014 Power losses prediction in poly-v belt transmissions: application to front engine accessory drives *Int. Gear Conf. 2014: 26th–28th August 2014, Lyon* (Elsevier) pp 1162–71

[49] Borin D and Stepanov G 2022 Magneto-mechanical properties of elastic hybrid composites *Phys. Sci. Rev.* **7** 1119–40

[50] Metsch P, Romeis D, Kalina K A, Raßloff A, Saphiannikova M and Kästner M 2021 Magneto-mechanical coupling in magneto-active elastomers *Materials* **14** 434